

# Parasitic Capacitance Associated With Inductive Sensors Used in MIT Imaging

Joe R. Feldkamp

**Abstract**—Magnetic induction tomography (MIT) has recently been accomplished using a single inductive sensor, but under the assumption that it behaves as an ideal inductor. When performing a scan with a sensing coil that typically consists of a collection of concentric circular PCB copper traces connected in series, small amounts of parasitic capacitance arise that contribute to measured tank circuit loss. Results of this work quantify the magnitude of parasitic capacitance and associated losses. For current inductive sensors, capacitance related loss is shown to diminish considerably when the coil is positioned more than  $\sim 2$  cm from a target boundary. Recognizing that single coil MIT scans generally position the coil within 2 cm of a target boundary, a correction is proposed that enables a more accurate measurement of true inductive loss. Previously published scan data over agarose phantoms are then reexamined to show the negative impact on imaging fidelity that results when capacitance related losses are ignored. Image comparisons are made using full 3D image reconstruction, demonstrating that failure to compensate for parasitic capacitance loss can degrade image fidelity.

**Index Terms**—Electrical Conductivity Distribution, Inductive Loss, Magnetic Induction Tomography, Scanning Single Coil MIT, Texas Instruments LDC-1101, Parasitic Capacitance

## I. INTRODUCTION

INDUCTIVE sensors used for single-coil MIT (magnetic induction tomography) imaging applications commonly consist of multiple loops of copper traces deposited on standard PCB (printed circuit board) substrates – essentially, multiple short solenoids connected in series [1]. An example is shown in Appendix C. Applied RF excitation creates a time-dependent electro-magnetic field that generates eddy currents at various locations within a nearby conductive target, dependent upon local conductivity. Eddy current generation requires that the original field do work to oppose eddy current fields, resulting in a measureable loss in the tank circuit that incorporates the inductor. Loss has been measured in a number of ways, with each method agreeing closely with an analytical result [1] that connects 3D conductivity with inductive loss. This has formed the basis of single-coil MIT imaging ([1]–[9]) on low conductivity materials such as biological tissues.

As is true of any inductor, non-ideal behavior is present, possibly impacting the quality of image reconstruction methods that ignore non-ideal behavior. The primary unwanted behavior is parasitic capacitance, including that due to inter-winding capacitance, but more critically, capacitance arising between any of the coil loops and nearby conductive objects – or, more generally, capacitance arising from an interaction between individual loops and the entirety of a coil's surroundings. Just as an inductor will have an associated loss due to eddy currents, the capacitance of a coil loop interacting with its environment will also have an associated loss due to charge

redistribution and movement on surfaces of nearby conductive objects.

A goal of this paper is to provide guidance on the extent to which these loss quantities – inductive and capacitive – can be differentiated and therefore made separate. Early sections of this paper provide an in-depth examination of the capacitance formed between a single annulus and a nearby conductive target, where both analytical and boundary element (BE) methods provide a good measure of the magnitudes of capacitance that might be expected. This is followed by a careful assessment of the loss associated with this capacitance and how overall tank circuit loss might be corrected for any capacitance related loss. Ultimately, the goal is to yield pure inductive loss, for which a quantitative analytical model [1] is available for image reconstruction. To build confidence in the capacitance models, experimental results are offered comparing capacitance predictions from the boundary element model with measurements. Finally, the proposed correction is used on existing single-coil scanning data for an agarose gel phantom to show the impact on image fidelity.

## II. CAPACITANCE OF A SINGLE ANNULUS

An important first step in evaluating coil-target capacitance is to compute capacitance for the simple case of a single annulus, relative to a grounded spherical shell located at infinity. Once obtained, this result will serve as the starting point for more general problems using boundary element methods.

A single coil loop consists of an annulus having infinitesimal thickness, with inner radius ' $a$ ' and outer radius ' $b$ ' – essentially, a circular trace on a PCB. Surface charge density is considered to have a uniform value,  $\alpha$ , across the

J. R. Feldkamp was previously with Kimberly-Clark, but is now with Tayos Corp., Louisville, CO 80027 USA (e-mail: jrfeld@tayoscorp.com).

Submitted August 31, 2022; Accepted...

entire annulus. Actual charge for a constant potential annulus is not distributed uniformly, but this assumption is shown later to have little impact on our results regarding capacitive loss. Solving the appropriate Poisson's equation using spatial Fourier Transform methods leads to the desired solution:

$$\psi_s(r, z) = \frac{\alpha}{2\epsilon} \left( b \int_0^\infty d\kappa J_1(\kappa b) J_0(\kappa r) \frac{e^{-|z-z_s|\kappa}}{\kappa} - a \int_0^\infty d\kappa J_1(\kappa a) J_0(\kappa r) \frac{e^{-|z-z_s|\kappa}}{\kappa} \right) \quad (1)$$

The annulus is located along the  $Z$  axis, at  $z = z_s$ . Using the same strategy, a slightly more difficult problem solves for the case of a uniformly charged annulus located on the  $Z$  axis, set at a distance  $z_s$  above a ground plane of zero potential:

$$\psi_s(r, z) = \frac{\alpha}{2\epsilon} \left\{ \begin{array}{l} b \int_0^\infty d\kappa J_1(\kappa b) J_0(\kappa r) \frac{(e^{-|z-z_s|\kappa} - e^{-|z+z_s|\kappa})}{\kappa} \\ - a \int_0^\infty d\kappa J_1(\kappa a) J_0(\kappa r) \frac{(e^{-|z-z_s|\kappa} - e^{-|z+z_s|\kappa})}{\kappa} \end{array} \right\} \quad (2)$$

From equations (1) or (2), annulus capacitance relative to either the ground plane or a grounded shell at infinity can be computed as:

$$C_r = \frac{\pi(b^2 - a^2) \alpha}{\psi_s(\frac{a+b}{2}, z_s)} \quad (3)$$

Charge density drops out of equation (3) when equation (1) or (2) is introduced. As expected, capacitance over a ground plane exceeds that relative to the infinite radius grounded shell, though the former approaches the latter as  $z_s \rightarrow \infty$ . As expected, the result for the annulus over a ground plane agrees with the disc result found in problem 3.21, page 142 of Jackson (3rd Ed.) [26] if  $a$  is set equal to 0 here, and if the Jackson result is specialized to a uniformly charged disk [26]. Capacitance of an annular loop over a ground plane is given in Figure 1 – loop radius to inner edge is either 2.0 or 4.0 cm, while trace width is 0.2 cm. Since the loop is likely in air over a target, relative permittivity was set to 1.0.

All calculations shown in Figure 1 evaluate the integrals found in equation (2) by subdividing the domain according to the zeroes of the first order Bessel function, with each subdivision handled using 8-point Gaussian quadrature – a total of 99,990 intervals led to 6-digit accuracy. Thus far, single-coil MIT experiments have only used annular rings with radii less than or equal to  $\sim 2.0$  cm (e.g. Appendix C).

Clearly, capacitance quickly decays to its free-space value, in agreement with values computed when using equation (1). Beyond  $\sim 2.0$  cm distant from the ground plane, capacitance changes very little, suggesting that any loss associated with the annular capacitor would be similarly consistent from one measurement to the next, allowing for easy subtraction. Unfortunately, single-coil MIT scan measurements most heavily rely upon inductive loss measurements taken within the 0.0 – 2.0 cm range. Thus, a better understanding of how short-range measurements are impacted by capacitance-related loss is needed. In comparison, multiple-coil MIT [10] may not have an issue with capacitance losses if coils are used at greater

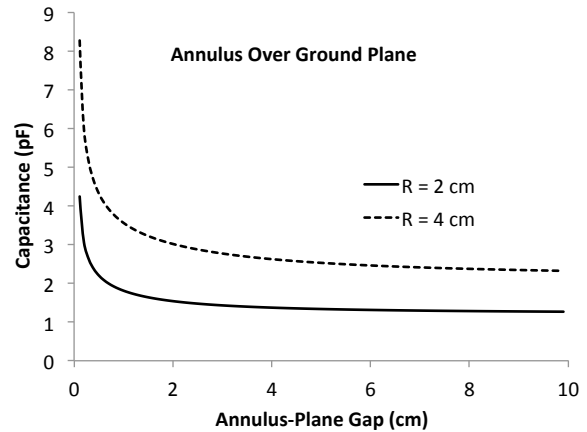


Fig. 1. Capacitance of annular rings over a ground plane; trace width is 0.2 cm – as reference, a metallic sphere of radius 2.0 cm has an isolated capacitance of 2.2 pF, while capacitance is 4.4 pF when spherical radius is 4.0 cm.

separations than that used in the single coil method. As an example, the setup described in [16] suggests that coils are used well outside the 2 cm limit indicated here and therefore may not be subjected to adverse capacitance effects.

### A. Annulus Capacitance Over Axisymmetric Bodies

Targets used in single-coil MIT are not well approximated by an infinite ground plane. Rather, finite, ungrounded targets are expected and may be less likely to facilitate charge build up on the annular rings of an induction coil. If so, this would be beneficial to image reconstruction from data acquired from single-coil MIT scans. Thus, this section considers capacitance calculations for annular rings over conductive axisymmetric bodies, either grounded or ungrounded. In either case, capacitance is simply defined as charge accrued on the target while grounded, divided by the ring potential at its midpoint. Ungrounded targets remain uncharged if originally discharged through momentary grounding. For sufficiently large targets however, charge distribution on a grounded target may not appear significantly different when grounded.

Though general targets can be treated by the methods of this section, axisymmetric targets are considered a useful first step to help better understand capacitance-related loss. Regardless of target geometry, electric charge will reside only on target surfaces. Thus, the target surface is an equipotential surface while the interior electric field is zero. In such circumstances, any variability of electrical conductivity or permittivity inside a target is immaterial. In order to qualify as a perfect conductor in a practical sense, the time constant for charge relaxation – the ratio of permittivity to electrical conductivity [11] – should be small compared to the electromagnetic field period. At 10 MHz, the human body may be treated as a perfect conductor for the sake of capacitance calculations.

Thus, the usual Poisson equation applies to the system under consideration:

$$\nabla^2 \psi = -\frac{\rho_s}{\epsilon_0} \quad (4)$$

Equation (4) applies to the entire region *outside* of the target. The target is at uniform potential – zero if grounded.

The charge density appearing in equation (4) is that due to the uniformly charged annulus, centered on the  $Z$ -axis and located at a distance  $z = z_s$  above the  $XY$  plane. The target is presumed to be located completely outside the space occupied by the annulus.

The response of the conductive target to the presence of the charged annulus is to accumulate charge across its surface – a net charge of zero if the conductor is left ungrounded. By superposition, the potential of equation (4) is written as the sum of two potentials – that due to the annulus charge, and the second due to the target's surface charge, which is distributed to ensure that boundary conditions are satisfied:

$$\psi(\vec{r}) = \bar{\psi}(\vec{r}) + \psi_s(r, z) \quad (5)$$

The second term on the right hand side of equation (5) is the potential from equation (1), obtained for a uniformly charged annulus, centered on the  $Z$ -axis with cylindrical coordinates  $r$  and  $z$ . Introducing equation (5) into equation (4) yields Laplace's equation for the potential  $\bar{\psi}$ , which may be written more conveniently as an integral equation over the target's bounding surface with the help of Green function  $w_i$ :

$$c_i \bar{\psi}(\vec{r}_i) = \int_{\partial R} da w_i \bar{\psi}_n - \int_{\partial R} da \bar{\psi} w_{in} \quad (6)$$

The constant  $c_i = \frac{1}{2}$  if the point  $r_i$  is exactly on the boundary  $\partial R$ , but unity if point  $r_i$  is off the boundary and thus outside of the target [27]. The Laplace free-space Green function is given by:

$$w_i = w(\vec{r}, \vec{r}_i) = \frac{1}{4\pi |\vec{r} - \vec{r}_i|} \quad (7)$$

Going forward, we specialize to targets that have cylindrical symmetry, and like the annulus, are centered on the  $Z$ -axis. With that restriction, the angular integrals within equation (6) can be separated and computed:

$$\int_{\partial R} da w_i \bar{\psi}_n = \int_{\Gamma} r ds \bar{\psi}_n \int_0^{2\pi} w_i d\varphi \quad (8)$$

The remaining integration is along the path  $\Gamma$ , formed by the intersection of the  $YZ$  plane with the target surface. And for the second boundary integral:

$$\int_{\partial R} da \bar{\psi} w_{in} = \int_{\Gamma} r ds \bar{\psi} \int_0^{2\pi} w_{in} d\varphi \quad (9)$$

The angular integral appearing in equation (8) is well known (Brebbia & Dominguez) [27]:

$$F(r, z, r_i, z_i) \equiv \int_0^{2\pi} w_i d\varphi = \frac{1}{\pi \sqrt{A+B}} K(k) \quad (10)$$

$K(k)$  is the complete elliptic integral of the first kind, with modulus  $k$ :

$$k = \sqrt{\frac{2B}{A+B}}; \quad A \equiv r^2 + r_i^2 + (z - z_i)^2; \quad B \equiv 2rr_i \quad (11)$$

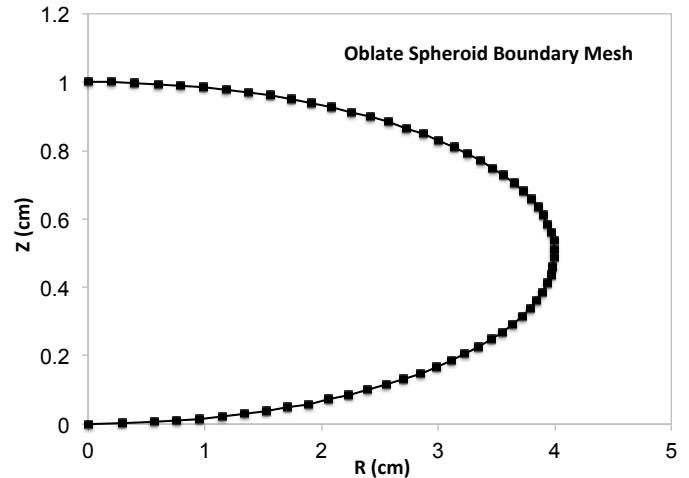


Fig. 2. An example of a boundary element mesh covering the right half of an oblate spheroidal body – 62 elements; integration path is taken as counter-clockwise. Large-axis diameter is 8.0 cm.

The remaining angular integral of equation (9) is obtained by taking the directional derivative of equation (10) along a surface unit normal, pointing to the target's interior – i.e., outward directed relative to the solution space. This is developed further in Appendix A. The Leibniz integral rule is used to permit interchange of differentiation with integration.

An example mesh of the remaining path for integration is shown in Figure 2 for an oblate spheroid. The  $Z$ -axis is coincident with the body axis. Because of symmetry, only one half of the boundary path requires a mesh. The example also illustrates a choice to use greater refinement where electrical charge has a greater tendency to accumulate, such as portions of higher curvature.

Returning to the boundary integral equation (6), we now have:

$$c_i \bar{\psi}(\vec{r}_i) = \int_{\Gamma} r ds \bar{\psi}_n F(r, z, r_i, z_i) - \int_{\Gamma} r ds \bar{\psi} F_n(r, z, r_i, z_i) \quad (12)$$

Subscript  $n$  indicates the directional derivative operation in the direction of the outward unit normal, i.e. toward the object's interior. Particular derivatives of the angular integral, needed to compute a directional derivative, are further illustrated in Appendix A.

Using equation (5) to incorporate the unknown potential function, we have:

$$c_i (\psi(\vec{r}_i) - \psi_s(\vec{r}_i)) = \int_{\Gamma} r ds (\psi_n - \psi_{sn}) F(r, z, r_i, z_i) - \int_{\Gamma} r ds (\psi - \psi_s) F_n(r, z, r_i, z_i) \quad (13)$$

Along the boundary, the potential is an unknown constant:  $\psi(\Gamma) = V_0$ . Surface charge on the object boundary,  $\sigma$ , is related to the normal derivative of the potential from  $\psi_n = -\sigma/\epsilon_0$ , provided the unit normal is directed out of the target, opposite to the normal direction we have already assigned for our boundary element formulation. Thus, the minus sign preceding surface charge density should be dropped. If not,

the determined surface charge density will simply be opposite what is expected. Introducing the surface charge and placing all unknown quantities onto the left hand side of equation (13), we have:

$$V_0(c_i + \int_{\Gamma} r ds F_{in}) - \int_{\Gamma} r ds \frac{\sigma}{\epsilon_0} F_i = c_i \psi_s(\vec{r}_i) - \int_{\Gamma} r ds \psi_{sn} F_i + \int_{\Gamma} r ds \psi_s F_{in} \quad (14)$$

Arguments of the function  $F(r, z, r_i, z_i)$  are suppressed in equation (14) in order to improve readability, but a subscript is appended as a reminder of dependence on location  $(r_i, z_i)$ .

Further progress requires specification of the types of basis functions that are used to represent surface charge  $\sigma$  along the boundary  $\Gamma$  shown in Figure 2, which illustrates an oblate spheroidal mesh. Though a variety of options are available, the simple choice of constant elements works well and is used here:

$$V_0(c_i + \sum_j \int_{\Gamma_j} r ds F_{in}) - \sum_j \frac{\sigma_j}{\epsilon_0} \int_{\Gamma_j} r ds F_i = c_i \psi_s(\vec{r}_i) - \sum_j \int_{\Gamma_j} r ds \psi_{sn} F_i + \sum_j \int_{\Gamma_j} r ds \psi_s F_{in} \quad (15)$$

Equation (15) includes an unknown surface charge density for each boundary segment, as well as a single unknown body potential. If the location  $(r_i, z_i)$  is repeatedly chosen at the center of each of the  $N$  boundary segments, then we have a system of  $N$  equations in  $N + 1$  unknowns – one unknown surface charge density per segment and the unknown body potential. An additional equation is therefore needed if we enforce charge neutrality over an ungrounded slab:

$$\int_{\partial R} \sigma da = 2\pi \int_{\Gamma} \sigma r ds = 0 \quad (16)$$

As before, cylindrical symmetry is assumed. Using constant element basis functions for surface charge density, equation (16) becomes:

$$2\pi \sum_j \sigma_j \int_{s_j}^{s_{j+1}} r ds = 0 \quad (17)$$

The remaining path-segment integrals are evaluated analytically. This additional equation (17) is not needed when the target body has been grounded, placing it at zero potential. The problem has been coded both ways so that solutions may be examined and compared.

Once the unknowns have been found, results are entered into equation (13) to permit a calculation of potential at any point in space outside the target:

$$\psi(\vec{r}_i) = \psi_s(\vec{r}_i) + \int_{\Gamma} r ds \left( \frac{\sigma}{\epsilon_0} - \psi_{sn} \right) F_i - \int_{\Gamma} r ds (V_0 - \psi_s) F_{in} \quad (18)$$

Known potential and surface charge densities are inserted into equation (18), and because the field point is outside the target,  $c_i = 1.0$ . Out of convenience, both equations (15) and (18) are scaled with the factor  $2\epsilon_0/\alpha$ , the reciprocal of the factor that precedes the integral in equation (1). After multiplication,

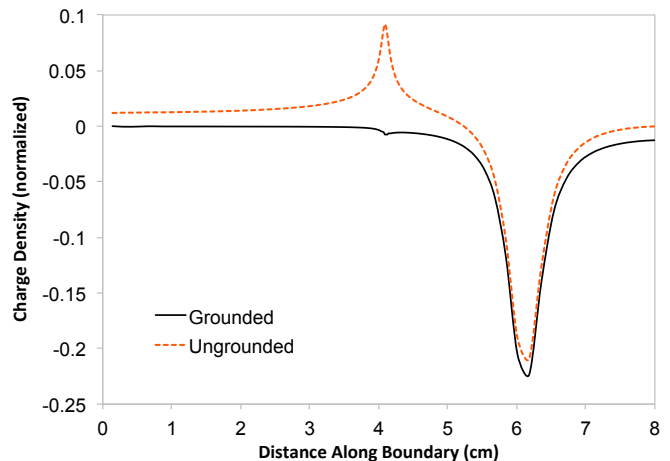


Fig. 3. Plot of normalized surface charge density along the path surrounding the 8 cm oblate spheroidal body. The bottom of the spheroid is at left, while the top of the spheroid, closest to the annulus, is at the right. The pronounced increase in negative surface charge density occurs beneath the positively charged annular ring.

the unknown and computed values become:

$$\begin{aligned} \text{unknowns} &: \left\{ \frac{\epsilon_0 V_0}{\alpha}; \frac{\sigma_j}{\alpha} \right\}; \\ \text{computed potentials} &: \left\{ \frac{2\epsilon_0 \psi(\vec{r}_i)}{\alpha} \right\} \end{aligned} \quad (19)$$

Thus, computed surface charge densities are scaled by the annulus surface charge density, and therefore dimensionless, while computed potentials have units of length – here, *cm* units are used (Note: the factor of 2 from the scaling factor does not appear together with the set of unknowns; only with external potential values.)

For the oblate spheroidal body illustrated in Figure 2, the surface charge density along the boundary was computed for the same annulus considered earlier in Figure 1 – inner radius of 2.0 cm and outer radius of 2.2 cm. The annulus was placed 0.2 cm above the top of the spheroidal body and dielectric constant set to 1.0. Surface charge density, normalized by the annulus charge density, is plotted in Figure 3 for both a grounded and ungrounded spheroidal body. The horizontal coordinate is the path distance along the body, starting at the bottom and moving counterclockwise to eventually reach the top.

Setting annulus charge density to 1.0 pC/cm<sup>2</sup>, annulus total charge is 2.639 pC, while total charge on the grounded oblate spheroid is -2.554 pC. When the body is grounded, annulus potential (at its midpoint) is 0.173 cm (0.977 volt). If ungrounded, the annulus potential rises to 0.310 cm (1.75 volt), while the body's potential is 0.0724 cm (0.41 volt). If the oblate spheroid is stretched two times along its horizontal axis, total charge on the grounded sphere becomes -2.592 pC, moving closer to the annular charge. Annulus potential when the body is grounded is 0.158 cm (0.892 volt). If ungrounded, the annulus potential is 0.234 cm (1.321 volt).

One measure of capacitance can now be computed from the scaled quantities as the amount of body-induced charge under grounded conditions, divided by the annulus potential needed

to achieve it, computed at its midpoint:

$$C = \frac{Q_b}{V_a} = \frac{2\epsilon_0\hat{Q}_b}{\frac{2\epsilon_0\psi_a}{\alpha}} = \frac{2\epsilon_0\hat{Q}_b}{\hat{\psi}_a} \quad (20)$$

A rationale for this definition is the expectation that capacitance related loss is only connected with target-induced charge distributions, as explained in the next section. Quantities with an over-carrot are directly computed with the BE model –  $\hat{Q}_b$  gives the amount of charge induced on the body, while grounded, due to annulus potential  $\psi_a$ . The former has units of squared-cm, while the latter has units of cm. Charge on the annulus itself is due to its interaction with all objects in its environment, and the definition above is meant to capture just the redistribution of charge on the nearby target. As the BE model shows, surface charge induced on the grounded target is nearly the same as annulus charge when annulus and target are very close.

According to the definition of equation (20), capacitance is 2.55 pF. If the entire charge of the annulus had been used instead, capacitance would have been 2.70 pF. This small capacitance difference indicates that interaction with the target dominates. Furthermore, the similarity between the two curves shown in Figure 3 suggests that the chosen oblate spheroid is already large enough to function as an adequate ground by itself – essentially, the spheroid equator and bottom function like a repository of charge.

If the oblate spheroid is made larger by stretching in the  $XY$  plane so that the long axis diameter is 16.0 cm instead of the 8.0 cm shown in Figure 2, capacitance is 2.906 pF. Again, if all annular charge were included in the calculation, capacitance would have been 2.960 pF. This even smaller difference shows that the annulus-target interaction dominates. Strong similarity between grounded and ungrounded curves again shows that larger conductive bodies experience charge redistribution as though they were grounded even if ungrounded. Of course, target-induced charge is expected to decrease substantially as the annulus-target distance increases. In that situation, induced charge will also become considerably smaller than the annular charge, indicating that annulus charge becomes more a consequence of its interaction with other features of its environment, in particular the hypothetical grounded spherical shell at infinity.

Obviously, the ungrounded spheroid has no net charge, so that the strong accumulation of negative charge just beneath the annulus location must be exactly counterbalanced by a corresponding amount of positive charge elsewhere. Clearly, the best location for storing the positive charge is at the spheroid's equator where curvature is highest and ample surface area is available, but also along the spheroid underbelly farthest from the annulus. Both are far from the positively charged annulus. Figure 4 shows the charge distribution for the larger, 16 cm diameter oblate spheroid. Clearly, the spheroid is now large enough that it behaves as its own ground – grounded and ungrounded curves are nearly the same, apart from the small positive spike along the side of the spheroid. Because the human body is much larger still, it too is expected to behave as an excellent ground when annular charge is small. Locations on the target body, farthest from the annulus, serve

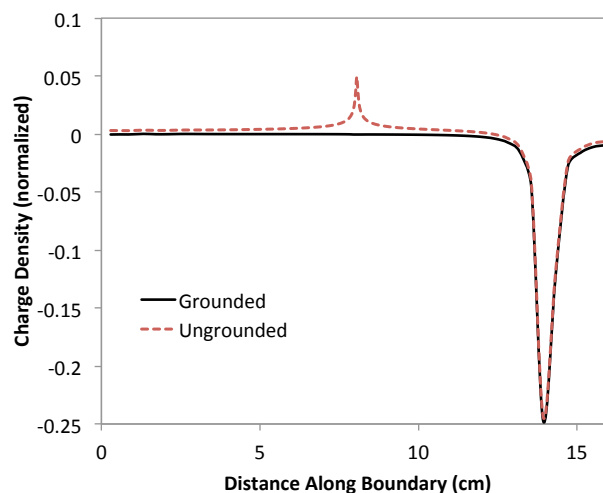


Fig. 4. Plot of normalized surface charge density along the path surrounding the 16 cm oblate spheroidal body. The bottom of the spheroid is at left, while the top of the spheroid, closest to the annulus, is at the right. The pronounced increase in negative surface charge density occurs beneath the positively charged annular ring.

as effective ground points, providing charge that gathers on the body surface beneath the annulus when nearby. The formation and dissipation of these surface charge distributions constitute the origin of capacitance-related losses. Additional measures of capacitance are considered in a later section.

### III. CAPACITANCE LOSS

This section considers capacitance-related losses associated with loop coils placed in the immediate vicinity of general conductive bodies. An ideal resonant tank circuit consists of an ideal inductor and ideal capacitor in parallel. Once the inductor is near a conductive target, however, a resistance appears in series with the inductance. Thus far, such resistance has been computed using an analytical formula developed for very short solenoids, arranged concentrically, and connected in series [1]. Experimental work has shown that agreement with experiment is essentially quantitative for conductivity values above  $\sim 0.2$  S/m, and over distances spanning from  $\sim 0.2$  cm out to a few cm [9].

For lower conductivity targets, especially biological tissues, the important conductivity range for imaging purposes is from  $\sim 0.05$  S/m up to  $\sim 1.5$  S/m [12]–[15]. Of concern here is the extent to which capacitance-related losses spoil the agreement with experiment when values fall into the lower portions of that range. As with the inductor, capacitance-related loss  $R$  will appear as a resistance in series with the capacitance  $C$  that naturally forms between coil loops and a nearby conductive target. An equivalent circuit representing the inductance and relevant capacitances, together with their associated losses is shown in Figure 5.

An additional capacitance  $C_g$  is shown in the circuit to represent the inevitable capacitance that also appears between instrumentation common traces and the conductive target. No attempt is made to compute this capacitance, though experimental measurements attempt to find an upper bound. Ideally,

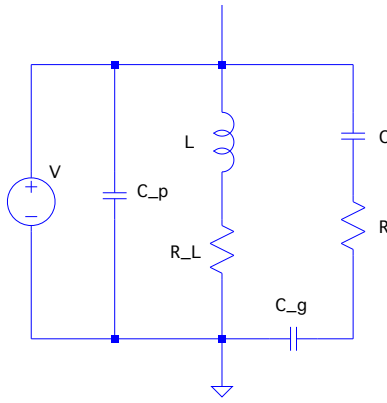


Fig. 5. Shows the key components of the  $LC$  tank circuit that contribute to loss;  $L$  is the sensor inductance,  $C_p$  is an added fixed capacitance needed for tuning;  $C$  represents the coil-target capacitance while  $R$  is a capacitive loss associated with the target; finally,  $C_g$  represents the “return” capacitance between instrumentation common lines and the target/environment.

this “return” capacitance would be small and help minimize the role that capacitive loss will play. When measuring the capacitance of the circuit in Figure 5,  $C_g$  is lumped together with  $C$  in a combined capacitance of  $C_g C / (C_g + C)$ . An additional capacitance needed to tune the circuit to a desired frequency is shown as  $C_p$ .

The admittance,  $Y$ , of the above circuit (considering  $C_g$  is lumped in together with  $C$ , and just written as  $C$  here) can be written down from elementary circuit analysis theory:

$$Y = G + iB = \frac{1}{R_L + i\omega L} + \frac{1}{R - i\frac{1}{\omega C}} + i\omega C_p \quad (21)$$

Current instrumentation based upon the Texas Instrument LDC1101 ([21], [22]) operates in resonance, so that  $B = 0$ . The real part of admittance is measured at resonance, together with resonant frequency, and is equal to:

$$G = \frac{R_L}{R_L^2 + \omega^2 L^2} + \frac{1}{R} \frac{\omega^2 R^2 C^2}{1 + \omega^2 R^2 C^2} \quad (22)$$

Of course,  $R_L$ ,  $R$  and  $C$  are not actual physical components of the circuit, but represent electromagnetic properties of the coil-target interaction. The coil-target portion of capacitance has been computed in previous sections, so the concern now is how to specify  $R$ . The product  $RC$  is directly related to the rate of charge formation or relaxation along a target boundary.

The continuity equation applies to any target location, and describes the charging or discharging process there:

$$\nabla \cdot \vec{j} + \frac{\partial \rho}{\partial t} = 0 \quad (23)$$

Introducing Ohm’s Law and Gauss’ Law, with the assumption that conductivity is nominally constant,

$$\frac{g}{\varepsilon} \rho(t) + \frac{\partial \rho}{\partial t} = 0 \quad (24)$$

A solution for equation (24), satisfying the initial condition that  $\rho(0) = \rho_C$ , is:

$$\rho(t) = \rho_C e^{-t/\tau_c} ; \quad \tau_c = \varepsilon/g \quad (25)$$

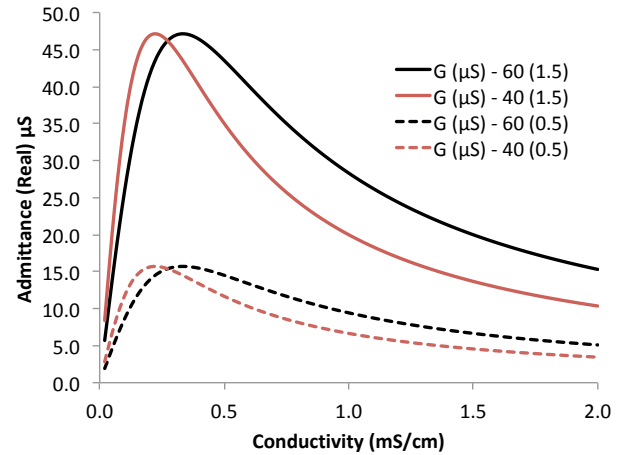


Fig. 6. Second term behavior of admittance at resonance from equation 26; applied frequency is 10 MHz and relative permittivity of either 40 or 60; capacitance  $C = 0.5$  or  $1.5$  pF

The time constant for charge relaxation (page 139 of [11]) provides a measure of the time required to form or dissipate surface charge on conductive targets. Here, we set this time constant equal to  $RC$ , providing a measure of capacitive loss associated with capacitance  $C$ ; i.e.,  $RC = \varepsilon/g$ . With this identification as time constant, equation (22) becomes:

$$G = \frac{R_L}{R_L^2 + \omega^2 L^2} + C \frac{\omega^2 (\varepsilon/g)}{1 + \omega^2 (\varepsilon/g)^2} \quad (26)$$

Since  $R_L \leq 1\Omega \ll \omega L$  in all cases of interest, and since theory shows  $R_L \propto g$ , the first term of equation (26) will always grow linearly with conductivity. For very small conductivity, the second term will also grow linearly with  $g$ . However, as conductivity continues to increase, the second term of  $G$  reaches a maximum and then decreases as  $1/g$ . Clearly, resistance  $R$  is more heavily influenced by target conductivities  $g \lesssim 2.0$  mS/cm, than the much higher conductivity of Cu traces associated with a coil – indeed,  $R \rightarrow 0$  as  $g \rightarrow \infty$ .

Second term behavior is illustrated in Figure 6 for two different values of relative permittivity while frequency is set equal to 10 MHz.  $C$  was set at either 0.5 pF or 1.5 pF. As expected, decreased capacitance suppresses the importance of capacitive loss. The figure also shows that increased relative permittivity shifts the curves toward higher conductivity.

In order to minimize the impact of the behavior shown in Figure 6, two strategies might be used – using a lower value of inductance so that the first term is increased; and, reducing loop-to-target capacitance as much as possible so that the second term is decreased, accomplished with reduced trace width. Inductances commonly used for single-coil MIT are  $\sim 2\mu\text{H}$ , so that for  $R_L \sim 1\Omega$ , the first term in equation (26) is  $\sim 63\mu\text{S}$ . Thus, the behavior illustrated in Figure 6 more likely causes problems at low conductivity. The role of  $C_g$  is to reduce the effective value of the capacitance  $C$  appearing in the equations.  $C_g$  may become larger when using a large ground plane on instrumentation PCB’s and even further increased by its connection to larger objects, such as

a battery or an external power supply. If  $C_g$  is large (tens of pF), then results of Figure 6 would indicate a more pronounced capacitance related loss contribution to total loss.

A further way to reduce  $C$  and thus minimize capacitive losses is to at least partially cancel the parasitic capacitance itself through appropriate feed back strategies. Examples of cancellation have been reported [17]–[20], though the essential idea can be traced back to neutralization of vacuum tube RF power amplifiers. Unfortunately, the stray capacitance developed during a single-coil MIT scan varies significantly – as demonstrated in Figure 8 of section 5.

The behavior of equation (26) has been observed in unpublished experiments in our lab that measure admittance as a function of conductivity. Once conductivity exceeds  $\sim 1.0$  mS/cm, linearity is obtained thereafter, but is preceded by a small “bump” in the data as Figure 6 anticipates.

#### IV. CAPACITANCE FOR 2-CONDUCTOR SYSTEM

This section offers an approach to help justify the use of constant annular charge density and a clarification of the relevant capacitance responsible for capacitive loss. For a system consisting of the two conductors – annular ring (1) and conductive slab (2) just beneath it, the charge on each can be written as a linear combination of the potentials on each [26]:

$$Q_i = \sum_{j=1}^2 C_{ij} V_j ; i = 1, 2 \quad (27)$$

Actually, instrument PCB common traces could be added in as a third conductor, but these are always assigned to zero potential and do not affect our analysis. In a first experiment that keeps the second conductor (target) at ground potential ( $V_2 = 0$ ; i.e. same as PCB common traces), equation (27) becomes:

$$C_{11} = \frac{Q'_1}{V'_1} \geq 0 ; C_{21} = \frac{Q'_2}{V'_1} \leq 0 \quad (28)$$

In a second experiment, body conductor 2 is initially grounded to remove all of its charge, but then disconnected from ground while conductor 1, charged as in the first experiment, is brought into the same position employed in the first experiment. Equation (27) then becomes:

$$Q''_1 = C_{11}V''_1 + C_{12}V''_2 ; 0 = C_{21}V''_1 + C_{22}V''_2 \quad (29)$$

Realizing that the capacitance matrix is symmetric,  $C_{12} = C_{21}$ . The remaining coefficient of capacitance  $C_{22}$  is found from the second result in equation (29) as:

$$C_{22} = -\frac{Q'_2}{V''_2} \frac{V''_1}{V'_1} \geq 0 \quad (30)$$

As a consistency check on BE solutions, the first of the equations from (29) can be rewritten, with the help of equation (28) and symmetry, as:

$$Q''_1 = Q'_1 = Q'_1 \frac{V''_1}{V'_1} + Q'_2 \frac{V''_2}{V'_1} \quad (31)$$

Results from the boundary element computations can be directly introduced into equation (31) to check for consistency. Equation (31) may also be divided by  $Q'_1$  to permit a simpler check on consistency:

$$1 = \frac{V''_1}{V'_1} + \frac{Q'_2 V''_2}{Q'_1 V'_1} \quad (32)$$

Clearly, the right hand side of Equation (32) should equal 1.0. Equation (31), however, was derived under the requirement that all components are true conductors, with each having an equipotential surface across their respective boundaries. That is not the case for the annular conductor included in the computation, which was assumed to have a uniform charge distribution. So, equation (31) or (32) could only be approximately satisfied. Nevertheless, in all computations reported here, the right hand side of equation (32) has remained in a range from 0.9990 to 1.0001, indicating that assigning a uniform charge density to the annulus is acceptable for capacitance calculations.

Using the oblate spheroid of Figure 2, and placing the annular ring 0.2 cm above the spheroid as before, we find that  $C_{11} = 2.70$  pF,  $C_{12} = -2.55$  pF and  $C_{22} = 5.47$  pF; the right hand side of equation (32) is 1.00006 (almost exactly 1.0 as required). If the spheroid is stretched two times along its horizontal axis, computed  $C_{11} = 2.96$  pF,  $C_{12} = -2.906$  pF and  $C_{22} = 8.746$  pF, which is not surprising since the spheroid has grown considerably in size. The capacitance defined by equation (20) is, in fact,  $C_{12}$  as specified here.

#### V. PARASITIC COIL CAPACITANCE OVER 2% KCl SOLUTION

In previous work, the inductive loss in a multi-loop coil (see Appendix C), placed above a 2% KCl solution contained inside a 14 cm diameter petri dish at a depth of 2 cm, was measured while manually moving the coil along the petri dish axis. The results of that experiment, together with theoretical predictions, are replotted in Figure 7 [9]. Though agreement with theory is excellent, we wish to explore the magnitude of the error committed by not including capacitance related losses, as proposed in equation (26) and graphically in Figure 6. The inductive loss shown in Figure 7 was measured using the Texas Instruments LDC1101 inductance to digital converter, which measures admittance of an  $LC$  tank circuit while in resonance – i.e., the left side of equation (26). However, only the first term of equation (26) was considered important when computing  $G$  from LDC1101 data.

To assess the omitted term, it is necessary to know the extra capacitance that forms across the  $LC$  circuit while the inductive sensor is moved along the petri dish axis. This is readily accomplished with the LDC1101 since it simultaneously measures the resonant frequency, which is nominally  $\sim 8.63$  MHz in this experiment. Since inductance is known, capacitance is easily calculated – in particular the capacitance in excess of that physically connected within the actual circuit. Since both inductive and capacitance-related losses are exceedingly small, setting the imaginary part of admittance,  $B$ , equal to zero results in the simple relation:

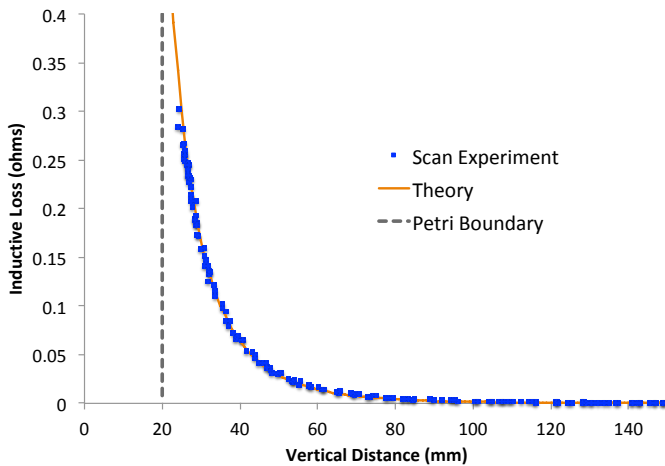


Fig. 7. Inductive loss in coil located at various positions above a 2% KCl solution, filling a 14 cm petri dish to a depth of 2 cm; the dashed vertical line locates the solution surface.

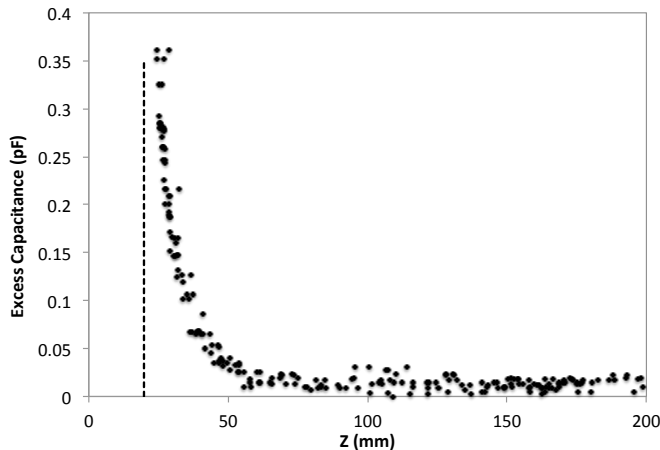


Fig. 8. Additional capacitance developed across the induction coil while translated along the petri dish axis, above its 2% aqueous KCl contents. This “excess” capacitance accounts for the two contributions depicted in Figure 5,  $C$  and  $C_g$ .

$$\omega = \frac{1}{\sqrt{L(C + C_p)}} \quad (33)$$

From  $\omega$ , the capacitance  $C$  is found, since other quantities in equation (33) are known. It is this excess capacitance that contributes to the two components ( $C$  and  $C_g$ ) of capacitance shown in the schematic diagram of Figure 5. Figure 8 shows the excess capacitance over the entire positioning range of the coil as it moves along the petri dish axis. It is only the excess capacitance that should be used in equation (26) or (34) introduced below, since capacitance obtained when the coil-to-target distance is large would not contribute to charge relaxation or dissipation within the nearby conductive target.

Since  $\epsilon$ ,  $g$  and  $\omega$  are all known for the petri dish experiment, the second term of equation (26) can be computed for each coil position. This is shown in Figure 9, together with a second axis indicating the equivalent inductive loss that should be considered as capacitance loss.

Noting that inductive loss ( $R_L$ ) is small compared with  $\omega L$ ,

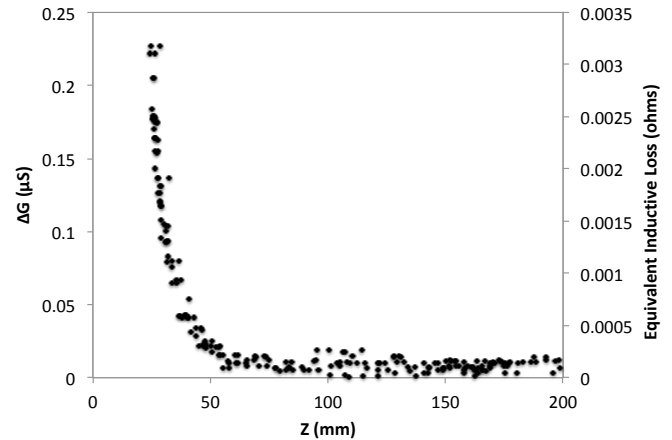


Fig. 9. A plot of the second term from equation (26), related to the capacitance loss contribution to admittance; the right hand axis shows the corresponding amount of loss as equivalent inductive loss – see equation (34).

we can directly solve equation (26) for the corrected inductive loss to give:

$$R_L = \omega^2 L^2 G - \omega^2 L^2 C \frac{\omega^2 (\epsilon/g)}{1 + \omega^2 (\epsilon/g)^2} \quad (34)$$

The second term appearing on the right hand side of equation (34) is a loss term not considered in arriving at the data presented in Figure 7. This missing amount is shown in Figure 9 via the right hand axis and contributes  $\sim 1\%$  to the inductive loss reported in Figure 7. Evidently, its contribution in this case is quite small and can be safely neglected. However, 2% KCl has a significantly higher conductivity than human body tissues, which nominally falls into the range from  $\sim 0.1$  to  $1.5$  S/m [12]–[15] while 2% KCl is  $3.2$  S/m. Note from Figure 6 that capacitance related loss only becomes minor for conductivities well above  $0.2$  S/m ( $2.0$  mS/cm). In the event that the second term in equation (34) is not negligible, equation (34) offers an approach for providing a better estimation of true inductive loss.

Finally, we use the BE model to help identify the magnitude of the “return” capacitance as represented by  $C_g$  in Figure 5. Figure 10 shows the mesh used to envelop the KCl solution contained within the petri dish. Placing the same annulus as used previously at a distance of  $0.2$  cm above the aqueous KCl target, charge density is computed from the BE model, and plotted in Figure 11.

Focusing only on the portion of the target surface located just  $0.2$  cm beneath the annulus, there isn’t much difference in the way that charge is distributed along the aqueous KCl target surface for grounded and ungrounded cases. Of course, the negative charge density in the ungrounded case must be compensated by positive charge elsewhere, which is accommodated by the small bumps at the corners and an additional small charge density along the bottom of the liquid target.

Figure 12 shows the computed capacitance of the annulus-petri system over a range of gap distances spanning from  $0.2$  cm up to  $10.0$  cm. The plot includes the previously shown results for the annulus over a ground plane, as well as the

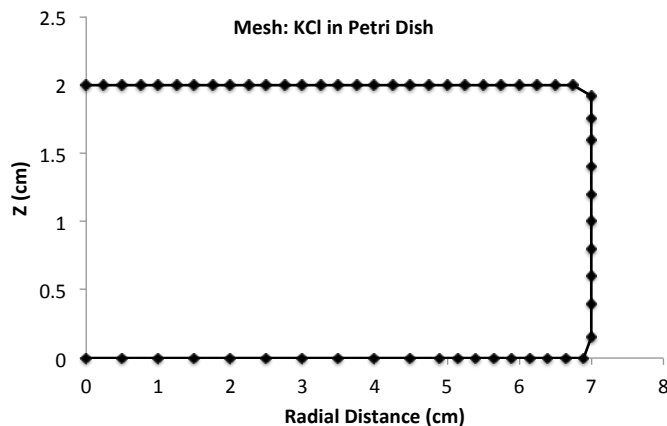


Fig. 10. Boundary element mesh for KCl solution contained within petri dish. Corners are somewhat beveled to lessen sharp-corner charge accumulation.

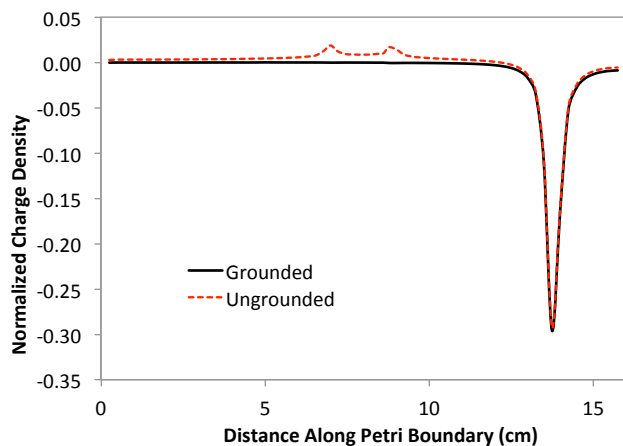


Fig. 11. Charge density along the perimeter of the aqueous KCl solution, which fills the petri dish to a depth of 2.0 cm. Annulus gap above solution is 0.2 cm. Notice the bumps of positive charge at the corners of the ungrounded target – needed to achieve net zero charge.

coefficients  $C_{11}$  and  $C_{12}$ . Annulus inner and outer radii are 2.0 and 2.2 cm respectively. Note that equations (1) and (3) predict an isolated annulus capacitance of  $\sim 1.20$  pF, which the  $C_{11}$  plot approaches asymptotically.

Of the capacitance definitions considered,  $C_{12}$  is specifically connected with the formation of charge on the conductive target – the only conductor where capacitance-related loss is expected to be significant, given the form of equations (26) and (34). Note that for metal PCB traces, where conductivity may be considered as infinite, the second term of either equation approaches zero.  $C_{12}$  directly captures the extent to which a charge distribution can arise on the grounded target in response to an electrical potential increase on the annulus. And since only redistribution of target charges will contribute to capacitance-related loss,  $C_{12}$  is regarded as the appropriate value for  $C$  in the schematic shown in Figure 5. Any additional annulus capacitance, such as that present when an annulus is isolated in space, cannot significantly contribute to loss.

As shown in Figure 12, the magnitude of  $C_{12}$  decreases quickly with distance from the salt-solution-petri target. If

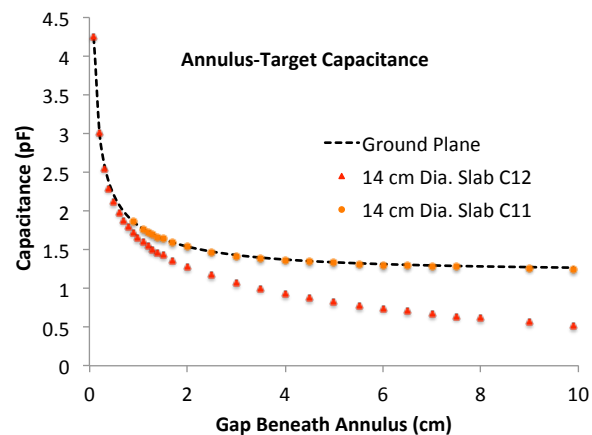


Fig. 12. Capacitance of annulus-target system as a function of gap distance between annulus and 14 cm diameter slab as meshed in Figure 10. Annulus has inner radius = 2.0 cm and outer radius = 2.2 cm. Infinite ground plane is shown for sake of comparison.

we let this annulus approximate the outer 2.0 cm loops of our PCB coil sensor (Appendix C), Figure 12 then provides an upper bound to what is measured, since there is still the additional capacitance  $C_g$  that serves as a return capacitance to instrument ground. Considering measured capacitance to be a combination of  $C$  and  $C_g$  connected in series, then the capacitance measured in Figure 8 must be controlled by  $C_g$  – in fact, the values in Figure 8 can be considered as a measure for  $C_g$ . This result is expected since the coil loops are usually much closer to the target than instrumentation ground paths. If the annulus trace width is increased to 0.4 cm, extending from 1.8 cm to 2.2 cm, capacitance increases to 3.973 pF when at a distance of 0.2 cm from the petri fluid. The situation could degrade however, leading to larger  $C_g$ , if the instrumentation PCB ground plane grows in area or if the instrument common is connected to extended external circuits.

Figure 12 also demonstrates the importance of  $C_{12}$  compared with  $C_{11}$ . The latter tracks the capacitance of the annulus over a ground plane and becomes asymptotic to the non-zero free space capacitance of the annulus, reflecting the interaction of an annulus with a grounded shell at infinity – which should not be considered in assessing loss via equation (26) or (34).

## VI. EXPERIMENTAL CAPACITANCE OF A THIN COPPER ANNULUS OVER PLAY-DOH™

To further validate the models and ideas of the previous sections, experimental measurements were made of the capacitance of an individual annular loop placed at various distances above a conductive phantom prepared from Play-Doh™, which has a conductivity  $\sim 3.0$  S/m. A direct comparison is then made with theoretical BE calculations.

The test annulus was prepared from 0.1 mm thick copper sheet cut to an inner diameter of  $\sim 5.50$  cm and outer diameter of  $\sim 6.35$  cm. Figure 13 shows the annulus bonded to a plastic petri lid resting  $\sim 3$  mm above a  $\sim 1.0$  cm thick slab of Play-Doh confined to a petri dish having a diameter of 8.6 cm.

Additional gap distance between the copper annulus and underlying Play-Doh was built up with a sequence of six

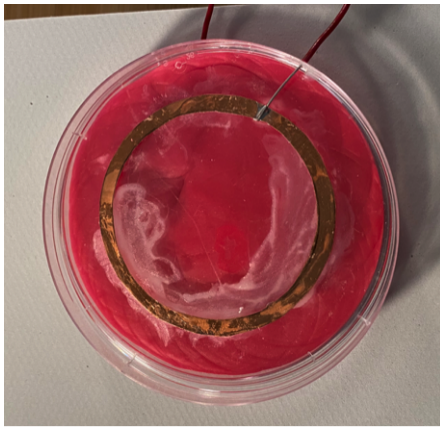


Fig. 13. Petri dish lid, with attached 0.1 mm thick copper annulus rests above 8.6 cm diameter petri dish, filled to a height of  $1.0 \pm 0.1$  cm with Play-Doh™.

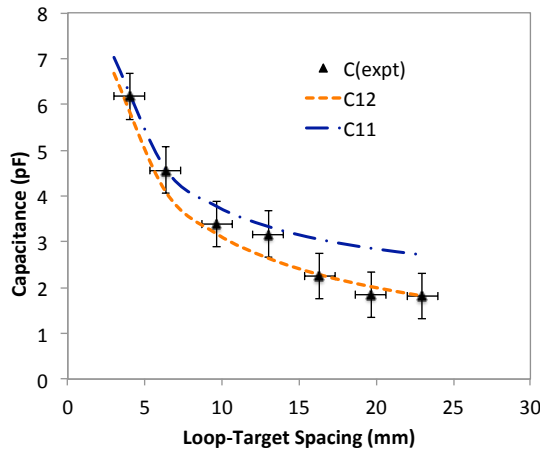


Fig. 14. Results from experiment that measure the capacitance of the annular loop, Play-Doh conductor system, shown together with theoretical computations.

0.33 cm thick EVA (ethylene vinyl-acetate co-polymer) foam sheets. Capacitance was obtained from two different pulse width measurements corresponding to insertion of two standard resistance values in series with the overall circuit. This permits subtraction of the unknown loss resistance of Play-Doh. The complete circuit then consists of the capacitance formed between the Play-Doh and copper annulus, as shown, together with one of the two sense resistors. The capacitance of the leads running from the setup to instrumentation was separately measured ( $\sim 8.5$  pF) and subtracted from the total system capacitance. The entire test setup rests on a 4.0 cm thick EVA foam slab, isolating the system of conductors.

Figure 14 shows the results of the seven measurements of annulus-Play-Doh capacitance, along with predicted values of  $C_{11}$  and  $C_{12}$  capacitance using the boundary element model discussed in previous sections. Error bars are shown on each of the data points, indicating the capacitance measurements over several replicates produced an error of  $\sim \pm 0.5$  pF and gap error of  $\sim \pm 1.0$  mm. Error is sufficiently small, while gap range is sufficiently large, that we can say with confidence that  $C_{12}$  is indeed the capacitance measured in this test.

## VII. EFFECTS OF CAPACITANCE LOSS CORRECTION ON MIT IMAGING

Given the strong similarity of Figures 7, 8 and 9, capacitive loss decays in a manner similar to inductive loss. Thus, it seems that the greatest benefit of including a loss correction due to parasitic capacitance might be to more accurately assess conductivity, but not necessarily gaining image quality improvement. Equivalently, failure to include losses due to coil-target capacitance may only produce an overestimate of electrical conductivity.

This question is tested here using a laboratory-created phantom, prepared from agarose [23], as previously described [9]. The phantom considered is contained in a 23 cm square petri dish, filled to a depth of  $\sim 2$  cm. Two 5.0 cm square  $\times$  2.0 cm tall agarose plugs are located along the petri diagonal, separated by a corner-to-corner gap of  $\sim 0.5$  cm. The remaining phantom space is filled to a depth of 2.0 cm with agarose having conductivity in the range  $\sim 0.05$  to 0.1 S/m. As described in [9] (open access), a hand-scan was performed that places the coil sensor at  $\sim 998$  locations in the immediate vicinity of the phantom surface while coil location is tracked to a precision of  $\pm 0.25$  mm (see Figures 4 and 13 of [9]). Tracking is accomplished using a surgical-suite IR camera from NDI ([4], [24]). As noted previously [9], hand placement ultimately leads to redundant sampling in numerous locations, while some regions are inadequately sampled, even though coil location is accurately known.

The choice of this particular data set for image reconstruction testing is motivated by a recent transition to the LDC1101 for measuring tank circuit losses. Previous electronics always imposed a fixed frequency on the coil sensor [1], while the LDC1101 does not. Fortunately, LDC1101 measurements also include resonant frequency, which varies due to parasitic capacitance changes. Thus, stray capacitance is measurable.

Scan data for this phantom is processed using full 3D image reconstruction, as described by Feldkamp [1] – the previous analysis [9] used 2D image reconstruction. Uncorrected inductive sensor loss data was first used for image reconstruction and then again after applying a correction, as indicated in equation (34). Applying a correction requires a value for the nominal phantom conductivity, as well as the phantom relative permittivity. The latter has been measured previously [6] as  $\sim 68$ , regardless of salt doping. Image reconstruction of uncorrected loss data leads to a nominal value of conductivity for the entire phantom, which is  $\sim 0.5$  S/m. With these two values available, Figure 15 shows a plot of the corrected loss, presumably now primarily inductive, against the uncorrected loss obtained from the LDC1101 chip.

As Figure 15 indicates, the amount of correction, given by the amount of departure from the dashed line, varies considerably over the 998 hand-scanned points. Though there appears to be no pattern, the amount of correction is most impacted by proximity to the agarose target. This expectation is approximately borne out in the plot given in Figure 16, which shows that the amount of correction generally grows as the phantom surface is approached more closely.

Even though Figure 16 shows that capacitance related loss

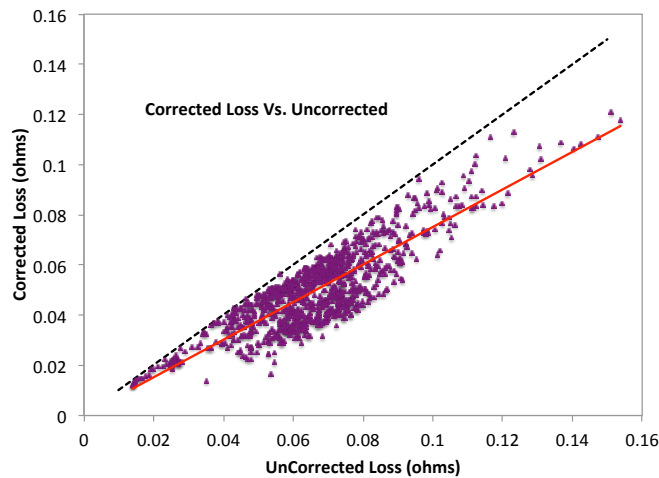


Fig. 15. Plot of capacitance-corrected loss against the uncorrected loss. Increased departure from the dashed line indicates greater correction.

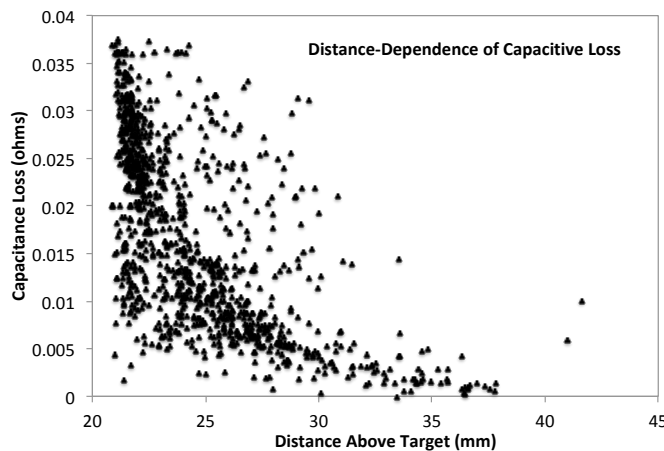


Fig. 16. Detailed look at how the correction due to capacitance-related loss depends upon distance between coil sensor and phantom.

follows a pattern of decrease as the sensor-phantom distance grows, there is still considerable noise. The amount of noise is sufficient to question whether image reconstruction would even benefit from loss correction.

3D Image reconstruction for the scan under examination is performed twice, once without capacitive loss correction and then again with correction. Image reconstruction uses Tikhonov regularization [1], which minimizes the sum of error and solution gradient penalty norms, the latter scaled by a smoothing parameter  $\lambda$ . An L-curve strategy was used to discern the most suitable value for  $\lambda$ , though the same value was obtained and used for either data set. Alternatively,  $\lambda$  may be set using a ‘discrepancy principle’ [25]. Alternative calculations were performed using a ‘shifted conductivity’ penalty norm [5], though conclusions reached here are not altered. More importantly, image reconstruction from single-coil MIT scan data requires an ‘instrumentation offset’ variable to serve as an unknown measure of the inductive loss approached asymptotically at infinite separation. Image fidelity is improved when this small offset is included.

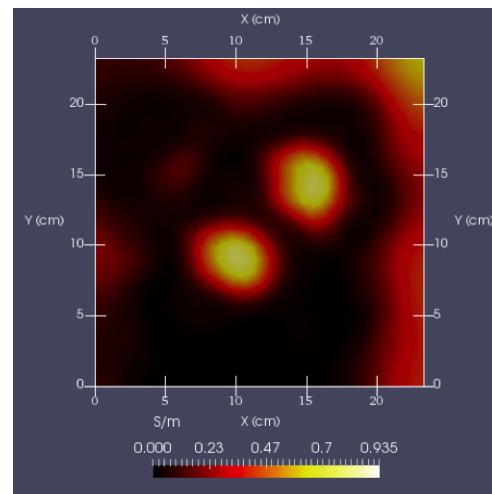
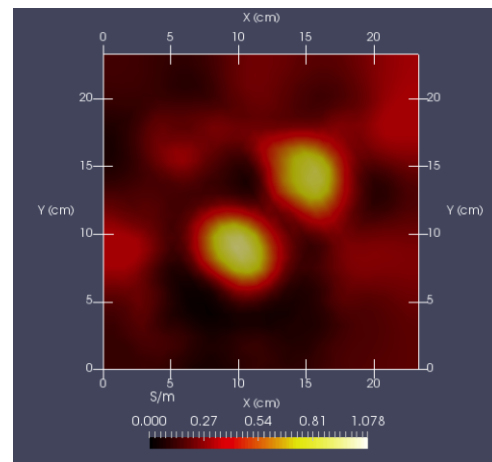


Fig. 17. Images obtained at slice  $Z = 1.0$  cm for reconstruction without capacitance loss correction (top), and with correction (bottom).

To facilitate objective comparison, identical slices through the reconstructed images are shown. The first slice is perpendicular to the phantom’s  $Z$ -axis at a location midway between phantom top and bottom horizons, i.e., at  $\sim Z = 1.0$  cm. This is shown for both uncorrected and corrected images in Figure 17. A simple linear 256-step color scale is used, transitioning from black at 0% to red at 33.3% to yellow at 66.6% and finally white at 100% full scale.

Comparison of images in Figure 17 reveal some significant differences in image fidelity. The conductive plugs are more readily discerned in the corrected image. Background conductivity is also more in line with the known small conductivity outside the plugs. There is some problem near petri boundaries, but this is mostly due to inadequate sampling near petri boundaries (Figure 13 of ref. [9]). Another difference is that conductivity trends higher in the absence of correction, which is expected. This all suggests that a reduction in coil-target capacitance is the preferable strategy for obtaining accurate inductive losses. Performing scans by hand-held maneuvering of an enclosure, with coil sensor attached, suggests a poor strategy, inasmuch as the conductive human body facilitates the development of capacitance between electronics and target. And this is in addition to the already problematic sampling en-

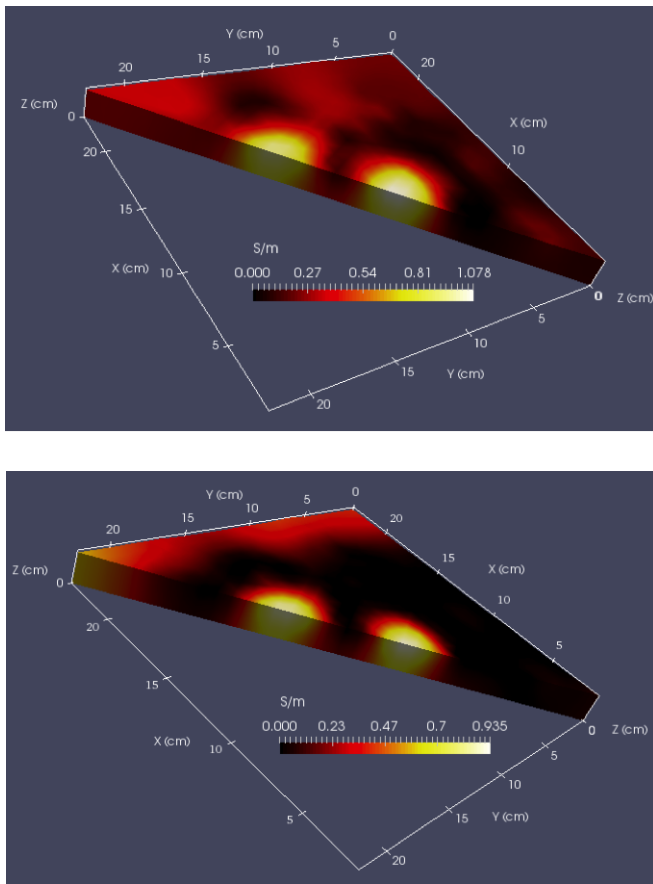


Fig. 18. Diagonal slices passing perpendicular to the XY plane of the phantom, comparing uncorrected (top) and corrected (bottom) images.

countered with hand sampling, where samples quickly become redundant, or locations are missed, as shown in [9].

The second slice examined is perpendicular to the XY plane of the phantom and passing through the diagonal axis that runs through the plug centers. These are shown in Figure 18, both for uncorrected and corrected conditions. Once again, correction for capacitance loss improves image fidelity, indicating better contrast between plugs and surroundings. And as before, the corrected image shows maximum conductivity values displaced downward by  $\sim 0.14$  S/m relative to uncorrected.

Figure 18, as well as 17, shows that features as small as the 0.5 cm gap can be resolved clearly along the entire Z-axis of the phantom, and even more so with capacitance loss correction. In the images, the gap appears to exceed the true corner-to-corner distance, and square plugs appear more rounded than square. This is commonly found with an image reconstruction approach that penalizes the solution gradient norm – sharp edges and corners are smoothed and rounded. Nevertheless the two plugs are distinct in both images.

In related work [5] involving virtual phantoms, where capacitance loss is absent, gap discernment was easily maintained up to the full depth of a 3.0 cm thick phantom for the same style coil sensor. There, the two inclusions were 3.8 cm wide  $\times$  1.8 cm thick strips buried in a 3.0 cm thick phantom. Separation was  $\sim 4.0$  cm and each spans the entire 16 cm length of the phantom. Buried conductive and nonconductive strips were

both considered, with the nonconductive strips meant to model bone embedded in muscle. As shown there, simulated bone strips were somewhat more easily resolved than conductive strips. That work, as well as the new work here, adds credence to the results reported in [1] showing an ability of single-coil MIT to approximately resolve bone structure along the thoracic spine, which lies only a short distance beneath the body surface. Correcting for capacitance related losses should help to further improve those images.

## VIII. APPENDICES

### A. Angular Integrals

The angular integral appearing in equation (9) follows directly from the angular integral developed in equation (10). For the case of axis-symmetric geometry, derivatives with respect to ‘r’ and ‘z’ are required. These are shown here:

$$\frac{\partial}{\partial z} \int_0^{2\pi} w_i d\varphi = -\frac{z - z_i}{\pi(A + B)^{3/2}} (K(k) + k K'(k)) \quad (35)$$

$$\begin{aligned} \frac{\partial}{\partial r} \int_0^{2\pi} w_i d\varphi = & -\frac{r+r_i}{\pi(A+B)^{3/2}} \\ & \times \left( K(k) - \frac{K'(k)}{k} \left[ \frac{2r_i}{r+r_i} - k^2 \right] \right) \end{aligned} \quad (36)$$

$$k = \sqrt{\frac{2B}{A+B}}; \quad A \equiv r^2 + r_i^2 + (z - z_i)^2; \quad B \equiv 2rr_i \quad (37)$$

Finally, the derivative of the complete elliptic integral  $K(k)$  can be written in terms of the complete elliptic integral of the second kind  $E(k)$ :

$$K'(k) = \frac{E(k)}{k(1-k^2)} - \frac{K(k)}{k} \quad (38)$$

In the event that the modulus  $k = \sqrt{2B/(A+B)}$  is very small, equation (38) is replaced by:

$$K'(k) = \frac{1}{4} \pi k (1 + 1.125 k^2) \quad (39)$$

Equation (39) results from the expansion of the complete elliptic integral  $K(k)$  and is used in calculations when  $k < 0.0001$ .

Once derivatives (35) and (36) have been obtained, the directional derivative of the potential  $\psi$  in some arbitrary direction given by the unit vector  $\hat{n}$  is found as:

$$\frac{\partial \psi}{\partial n} = \nabla \psi \cdot \hat{n} = \frac{\partial \psi}{\partial r} n_r + \frac{\partial \psi}{\partial z} n_z \quad (40)$$

A unit vector, normal to the conductive target, and directed toward the interior of the target is given by:

$$\hat{n} = (n_r, n_z) = (-\sin \beta, \cos \beta) \quad (41)$$

Equation (41) is appropriate for a counterclockwise path around the object. A unit tangent vector, pointing along a segment or element in the counterclockwise direction is similarly given by:

$$\hat{T} = (t_r, t_z) = (\cos \beta, \sin \beta) \quad (42)$$

TABLE I  
SYMBOLS APPEARING WITHIN THE ARTICLE

Symbol	Quantity	Typical Units
$\rho(\vec{r})$	charge density	coulomb/cm <sup>3</sup>
$g(\vec{r})$	electrical conductivity	Siemens/m, or (S/m)
$\vec{j}$	current density	pC/cm <sup>2</sup> sec
$r$	radial distance	centimeters, or cm
$C$	capacitance	pF
$z$	distance from XY plane	centimeters, or cm
$Y$	Admittance	$\mu$ S
$\epsilon$	permittivity	F/m
$\omega$	field angular frequency	$\pi$ radians/second
$\alpha, \sigma$	surface charge density	pC/cm <sup>2</sup>
$\psi_s, \psi$	electrostatic potential	volts
$V_0$	target potential	volts

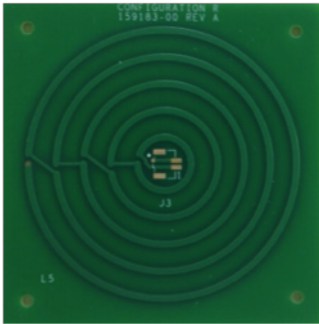


Fig. 19. Two-layer, PCB coil sensor, consisting of 5 Cu traces per layer; each trace is 1.0 mm wide; loop radii – 0.4, 0.8, 1.2, 1.6, 2.0 cm.

The two components are directly computed from boundary segment vertices:

$$\cos \beta = \frac{\Delta r}{\Delta s}; \quad \sin \beta = \frac{\Delta z}{\Delta s}; \quad \Delta s = \sqrt{\Delta z^2 + \Delta r^2} \quad (43)$$

## B. Table of Symbols

Table 1 provides a partial listing of some of the symbols used throughout. Units are also indicated in the last column.

## C. PCB Coil Geometry

The PCB-based coil sensor used in all experiments described in this paper is shown in Figure 19. There are two layers, separated by  $\sim 0.5$  mm, while each layer consists of five loops of Cu at the radii indicated.

## REFERENCES

- [1] J. R. Feldkamp, "Single-coil magnetic induction tomographic three-dimensional imaging", *J. Medical Imaging*, vol 2, no.1, 013502, (2015)
- [2] J. R. Feldkamp and S. Quirk, "Validation of a convolution integral for conductivity imaging", *Progress in Electromagnetic Research Letters*, vol. 67, pp. 1-6, (2017). 896-913, (2012)
- [3] J. R. Feldkamp and S. Quirk, "Effects of tissue heterogeneity on single-coil, scanning MIT imaging", *Proc. SPIE 9783, Medical Imaging: Physics of Medical Imaging*, 978359 (2016).
- [4] J. R. Feldkamp and S. Quirk, "Optically tracked, single-coil, scanning magnetic induction tomography", *Proc. SPIE 10132, Medical Imaging: Physics of Medical Imaging*, 10132172, (2017).
- [5] J. R. Feldkamp, "Inversion of an Inductive Loss Convolution Integral for Conductivity Imaging", *Progress in Electromagnetic Research B*, vol. 74, pp. 93-107 (2017).
- [6] J. R. Feldkamp and S. Quirk, "Coil Geometry Effects on Single-Coil Magnetic Induction Tomography", *Physics in Medicine and Biology*, vol. 62, pp. 7097-7113, May (2017).
- [7] J. R. Feldkamp and S. Quirk, "Internal Magnetic Induction Tomography Using a Single Coil", *Progress in Electromagnetic Research*, vol. 164, pp. 97-107, (2019).
- [8] J. R. Feldkamp and S. Quirk, "Optically tracked, single-coil, scanning magnetic induction tomography", *J. Medical Imaging*, vol. 4, no. 2, 023504, (2017).
- [9] J. Feldkamp and S. Quirk, "Single-Coil Magnetic Induction Tomography Using the LDC-1101 Chip", *IEEE Sensors Journal*, vol. 21, no. 1, pp. 633-641 (2021).
- [10] H. Y. Wei and M. Soleimani, "Electromagnetic tomography for medical and industrial applications: challenges and opportunities", *Proc. IEEE*, vol. 101, pp. 559-564, (2013).
- [11] J. R. Reitz and F. J. Milford, *Foundations of Electromagnetic Theory*, 2nd Edition, Addison-Wesley Publ. Co., p. 139, Reading Mass. (1967).
- [12] S. Gabriel, R.W. Lau and C. Gabriel, "The dielectric properties of biological tissues: II. Measurements in the frequency range 10 Hz to 20 GHz", *Phys. Med. Biol.* 41, pp. 2251-2269, (1996).
- [13] M. T. Joines, Y. Zhang, C. Li and R. L. Jirtle, "The measured electrical properties of normal and malignant human tissues from 50 to 900 MHz", *Medical Physics*, vol. 21, no. 4, pp. 547-550 (1994).
- [14] H. Wang et. al., "Dielectric properties of human liver from 10 Hz to 100 MHz: normal liver, hepatocellular carcinoma, hepatic fibrosis and liver hemangioma", *Bio-medical Mats. Engin.*, vol. 24, pp. 2725-2732, (2014).
- [15] R. Delonzor, R.K. Spero and J.J. Williams, "The electrical conductivity of in vivo human uterine fibroids", *Int. J. Hyperthermia*, vol. 27, no. 3, pp. 255-265 (2011).
- [16] B. Dekdouk, C. Ktistis, D. W. Armitage and A. J. Peyton, "Absolute imaging of low conductivity material distributions using nonlinear reconstruction methods in MIT", *Progress in Electromagnetics Res.*, vol. 155, pp. 1-18, (2016)
- [17] S. Wang and F. C. Lee, "Analysis and Applications of Parasitic Capacitance Cancellation Techniques for EMI Suppression", *IEEE Trans. on Industrial Electronics*, vol. 57, no. 9, pp. 3109-3117, (2010).
- [18] C. Hebedean, C. Munteanu, A. Racasan and O. Antonescu, "Parasitic Capacitance Cancellation for EMI Filters With an Embedded Ground Plane", *Annals of the University of Craiova, Electrical Engineering Series*, No. 35, pp. 13-18, (2011).
- [19] T. C. Neugebauer and D. J. Perreault, "Parasitic Capacitance Cancellation in Filter Inductors", *IEEE Trans. Power Electron.*, vol. 21, no. 1, pp. 282-288, (2006).
- [20] G. Dong and F. Zhang, "Equivalent Parallel Capacitance Cancellation of Common Mode Chokes Using Negative Impedance Converter for Common Mode Noise Reduction", *J. of Power Electronics*, vol. 19, No. 5, pp. 1326-1335, (2019).
- [21] SNOSD01D, "LDC1101 1.8-V High-Resolution, High-Speed Inductance-to-Digital Converter," May 2015, revised October 2016 by Texas Instruments, Dallas TX.
- [22] T. C. Chou, "Wearable Inductive Damping Sensors for Skin Edema Quantification", Dissertation (Ph.D.), Cal. Inst. of Technology. doi:10.7907/q77f-me73. <https://resolver.caltech.edu/CaltechTHESIS:01152020-143207091> (2022).
- [23] M. Kandadai, J. L. Raymond and G. J. Shaw, "Comparison of electrical conductivities of various brain phantom gels: developing a brain gel model", *Mater. Sci. Eng. C Mater. Biol. Appl.*, vol. 32, no. 8, pp. 2664-2667, (2012).
- [24] Wiles, A. D., Thompson, D. G., and Frantz, D. D, "Accuracy assessment and interpretation for optical tracking systems", *Medical Imaging Proceedings (SPIE)*, 5367, (2004)
- [25] M. Donatelli, A. Neuman, and L. Reichel, "Square regularization matrices for large linear discrete ill-posed problems", *Numerical Linear Algebra with Applications*, Vol. 19, pp. 896-913, 2012.
- [26] J. D. Jackson, *Classical Electrodynamics*, 3rd Edition, John Wiley & Sons, Inc., (1999).
- [27] C. A. Brebbia and J. Dominguez, *Boundary Elements, An Introductory Course*, Second Ed., McGraw-Hill Book Company, New York, NY (1992).